Research Square

Preprints are preliminary reports that have not undergone peer review.
They should not be considered conclusive, used to inform clinical practice,
or referenced by the media as validated information.

Small-scale mixing regulates the reconfiguration of the Arabian Sea oxygen minimum zone

Mauro Pinto-Juica

mauro.pinto.j@gu.se

University of Gothenburg

Leo Middleton

University of Gothenburg

Estel Font

University of Cape Town

Anneke ten Doeschate

Rockland Scientific Inc.

Bastien Queste

University of Gothenburg

Article

Keywords:

Posted Date: November 17th, 2026

DOI: https://doi.org/10.21203/rs.3.rs-11470115/v1

License: This work is licensed under a Creative Commons Attribution 4.0 International License.
Read Full License

Additional Declarations: No competing interests reported.

Small-scale mixing regulates the reconfiguration of the Arabian Sea oxygen minimum zone

Mauro Pinto-Juica[1*], Leo Middleton[1], Estel Font[1,2,3], Anneke ten Doeschate[4], Bastien Y. Queste[1]

[1]Department of Marine Sciences, University of Gothenburg, Gothenburg, Sweden.
[2]Department of Oceanography, University of Cape Town, Cape Town, South Africa.
[3]Southern Ocean Carbon-Climate Observatory, CSIR, Cape Town, South Africa.
[4]Rockland Scientific, Inc., Victoria, BC, Canada.
[*]Corresponding author: Mauro Pinto-Juica mauro.pinto.j@gu.se

Abstract

Oxygen minimum zones limit marine habitats and influence climate through carbon sequestration and greenhouse gas production. Studies suggest that long-term shifts in the balance between oxygen consumption and supply may “reconfigure” these regions across oxygen classes, with moderately oxygenated waters expanding while the most oxygen-depleted cores shrink. However, the mechanisms responsible for redistributing oxygen across classes remain unknown. Here we show, using high-resolution glider observations in the Arabian Sea, how distinct oxygen sources and small-scale mixing together act to shape the oxygen-class structure. Subsurface oxygen production at a deep chlorophyll maximum, mixed-layer deepening, and laterally advected Persian Gulf Water preferentially ventilate different oxygen classes, with seasonally varying contributions. Double-diffusive convection, a type of ocean mixing, accounts for >70% of the estimated oxygen redistribution. Idealized diffusion experiments show that mixing alone can produce changes in oxygen-class structure comparable in magnitude to longer-term modeled and observed shifts, with the resulting distribution strongly dependent on how mixing is represented. Reliable projections of oxygen minimum zone reconfiguration require Earth system models to represent local oxygen sources and the spatial relationship between small-scale mixing and oxygen gradients.

Introduction

The oceanic oxygen distribution is controlled by large-scale circulation patterns that transport oxygen-rich waters from their formation regions into the ocean interior[1–3]. Along these pathways, oxygen is progressively consumed by biological respiration, leading to the formation of Oxygen Minimum Zones (OMZs), when physical oxygen supply rates are insufficient to balance biological oxygen demand rates[4–7]. Although they occupy only a small fraction of the ocean volume[3,8], OMZs exert a disproportionate influence on marine ecosystems, biogeochemical cycles and climate by compressing macrofauna habitats[9] and modifying carbon[10–12] and nitrogen cycling[13–15]. Climate-driven changes in circulation, stratification, oxygen solubility and biological activity within and above OMZs are expected to reshape the structure and oxygen distribution of OMZs[3,6]. Recent modelling studies suggest that OMZs will experience a "reconfiguration" across oxygen classes[16,17], with moderately oxygenated waters (20–120 μmol kg^{-1}) expanding while the most oxygen-depleted cores (<20 μmol kg^{-1}) contract[18]. This reconfiguration is important because different oxygen classes support distinct ecological and biogeochemical processes. Expansion of the hypoxic waters (<60 μmol kg^{-1}) is associated with habitat compression for macrofauna[19,20] and greater carbon export and burial[10–12], whereas changes in the OMZ core directly influence nitrogen loss and the production of greenhouse gases such as N_2O[13,21]. Predicting the future evolution of OMZs requires understanding both the pathways via which oxygen enters these regions (oxygen sources) and the physical processes (e.g. mixing) that redistribute it within them.

The Arabian Sea hosts one of the most intense OMZs in the global ocean[22,23]. In the Sea of Oman, upper-ocean oxygen structure (<500 m depth) reflects the interaction of contrasting water masses, seasonal forcing and biological processes[24–27]. Surface layers are occupied by Arabian Sea High Salinity Water (ASHSW), whereas denser Indian Central Water (ICW; cooler, fresher and oxygen depleted) dominates at depth (below 300 m)[24,28]. Between these two water masses, warm, saline and oxygen-rich Persian Gulf Water (PGW) enters the northwestern Arabian Sea as a density-compensated outflow[26,29], providing a lateral source of oxygen to the OMZ[30]. Mesoscale circulation modulates PGW transport, producing substantial spatial and temporal variability in intermediate-depth oxygen distributions[26]. Seasonal forcing further modifies the upper OMZ boundary by altering the depth and vertical oxygen gradient of the upper oxycline[27,31–33]. Together, these sources introduce oxygen at different depths and timescales, generating strong variability within the upper OMZ.

Although stratification and circulation determine OMZ geometry, ventilation of oxygen-deficient waters depends on the mixing processes that redistribute the supplied oxygen. While large-scale circulation and oxygen gradients are increasingly well resolved by profiling floats[33,34] and modelling[19,35], the small-scale processes controlling vertical

oxygen distribution across oxygen classes, and their contribution to shaping the OMZ structure are not constrained. Below the energetic surface layer, shear-driven turbulence weakens and other mixing processes can become important[36,37]. Double diffusive convection (DDC), is a type of ocean mixing driven by the differential molecular diffusion of heat and salt that releases background potential energy[38], and can efficiently transport dissolved tracers such as oxygen[39–41]. In the Arabian Sea, DDC has been suggested to be one of the main mixing mechanisms[30], yet it remains unclear how this process contributes to modifying the oxygen-class structure across the OMZ.

Here, we use high-resolution underwater-glider observations from the northwest Arabian Sea to show how distinct oxygen sources and small-scale mixing together shape the oxygen-class structure of the OMZ. We identify three distinct oxygen sources: local production in a deep chlorophyll maximum (DCM), seasonal ventilation from mixed-layer deepening and lateral advection of PGW. By combining direct microstructure measurements with oxygen observations, we show how small-scale mixing redistributes oxygen from each source, with DDC dominating this redistribution. Each source preferentially ventilates distinct oxygen classes as its relative importance changes seasonally. Idealized diffusion experiments further show that small-scale mixing alone can substantially alter the oxygen-class distribution, with the resulting changes depending on how mixing is represented. Together, these results show how oxygen sources and mixing partition oxygen supply across classes and seasons, contributing to the short-term evolution of the OMZ.

Hydrographic structure and oxygen sources into the Arabian Sea OMZ

The data were collected with an underwater glider equipped with turbulence and current velocity sensors which surveyed the Sea of Oman from November 2024 to February 2025, capturing the seasonal transition in oxygen supply to the upper 500 m of the OMZ (Fig. 1). In November–December, biological production associated with a DCM maintained a ~25 m thick layer of moderately oxygenated water (60–150 μmol kg^{-1}; Supplementary Fig. S1) along the upper OMZ boundary. As winter mixing deepened the mixed layer to 135 m in January, the DCM disappeared and the 60 μmol kg^{-1} isopleth deepened and aligned with the mixed-layer base, shifting the dominant upper-OMZ oxygen source from subsurface biological production to direct surface ventilation.

Advection of PGW provides a third distinct oxygen source[24,29], forming density-compensated filaments with positive oxygen anomalies exceeding 10 μmol kg^{-1} and reaching up to 40 μmol kg^{-1}. Strong currents (>1.0 m s^{-1}) were associated with PGW outflows across a range of density classes (~25.4-26.4 kg m^{-3}; Fig. 1d), increasing spatial and temporal variability in the OMZ oxygen distribution (Fig. 1 and 2).

Mixing regimes governing vertical oxygen redistribution

The oxygen supplied to the Arabian Sea OMZ is redistributed by mixing processes whose efficiency depends on local energetic, stratification and thermohaline conditions. Using direct turbulence measurements and a set of nondimensional parameters describing the thermohaline and dynamical stability of the water column (see Methods), we identify three main mixing regimes (Fig. 2): ***(1)*** Energetic shear-driven turbulence under high buoyancy Reynolds numbers ($\mathrm{Re_b}$ >> 100), where oxygen is transferred across density surfaces through turbulent overturns[42]; ***(2)*** differential mixing under low-energy and strongly stratified environments ($\mathrm{Re_b}$ << 100), where the shear-driven diffusivity of dissolved tracers is strongly suppressed relative to fully developed turbulence[43,44]; and ***(3)*** DDC, where energy and background shear remain weak ($\mathrm{Re_b}$ << 100 and Richardson number, Ri>1) relative to the stratification but the local thermohaline structure is favorable to double diffusive processes (density ratio, $1/3 < \mathrm{R_\rho} < 3$)[45], efficiently transferring oxygen across isopycnals. As these processes produce diffusivities that differ by orders of magnitude, identifying the dominant mixing regimes is essential for understanding how oxygen supplied to the OMZ is redistributed across different oxygen classes. Because our focus is on mixing-driven oxygen redistribution within and above the OMZ, the analysis is restricted to waters below the mixed layer and within the upper 500 m.

The resulting mixing regime distribution reveals a vertical and temporal organization within the upper OMZ (Fig. 2c; see also Supplementary Fig. S2). Energetic shear-driven turbulence is concentrated within intense PGW filaments where enhanced shear occurs along the layered thermohaline structure, and near the seafloor over the shelf and slope. Differential mixing is found directly below the mixed layer, where turbulent energy is low and stratification remains strong. In contrast, DDC is concentrated within PGW-influenced waters and near the base of the deep winter mixed layer (Fig. 2c; see also Supplementary Fig. S3).

These spatial patterns translate into distinct mixing regime dominance among the three oxygen sources described in the previous section (Supplementary Fig. S2). Within the DCM, differential mixing dominates (~77% of observations), while DDC and energetic turbulence account for ~15% and <8%, respectively. Within PGW-influenced waters (PGW fraction > 0.15; see Methods) differential mixing and DDC account for ~51% and ~38% of observations, whereas energetic turbulence accounts for ~11%. However, within the intense PGW filaments (PGW fraction > 0.3; Supplementary Fig. S1d), locally enhanced shear increases the occurrence of energetic turbulence to ~24%, leading to alternating regimes of DDC and shear-driven mixing. During winter, when the mixed layer deepens and approaches the upper OMZ boundary, differential mixing and DDC are the dominant mixing regimes (~57% and ~29%, respectively).

The impact of each mixing regime on oxygen redistribution depends on both the diffusivity it generates and the oxygen gradient across which it acts. Differential mixing occupies a large fraction of the water column and often coincides with strong oxygen gradients, but its weak diffusivities (median 0.09 x 10^{-5} m^2 s^{-1} below the mixed layer over the whole campaign; Supplementary Fig. S4) result in limited vertical oxygen transport. Shear-driven turbulence produces the highest diffusivities (median 2.37 x 10^{-5} m^2 s^{-1} below the mixed layer over the whole campaign) but often occurs in well-mixed regions with weaker gradients, reducing its overall contribution to diapycnal oxygen fluxes. DDC combines both moderate to high diffusivities (median 1.20 x 10^{-5} m^2 s^{-1} below the mixed layer over the whole campaign) with strong oxygen gradients, resulting in an important contribution to the oxygen flux (Fig. 3c). This contrast is evident within the DCM, where differential mixing dominates, limiting the overall oxygen redistribution from this source, except within localized DDC-favorable layers that enhance oxygen fluxes across the upper OMZ boundary (Fig. 3b). Within PGW-influenced waters, DDC persists over a broader vertical extent. Consequently, the oxygen gradients created by laterally transported PGW are efficiently redistributed to the OMZ interior (Fig. 3b and c). DDC therefore emerges as the predominant regime redistributing the oxygen supplied through the DCM, winter ventilation, and PGW. In the following section, we quantify the resulting diapycnal oxygen fluxes to determine how these oxygen sources and mixing regimes together contribute to ventilating and shaping the oxygen class structure within the OMZ.

Diapycnal oxygen fluxes and OMZ reconfiguration

Recent studies predict that different oxygen classes within OMZs may evolve differently; while moderately oxygenated waters expand, the most oxygen-depleted cores may contract[16,17]. Such reconfiguration reflects a shifting long-term balance between oxygen consumption and oxygen supply rates. Here, we isolate the mixing-driven component and distinguish oxygen redistribution —the mixing-driven transfer of oxygen from individual sources across oxygen classes— from reconfiguration —the longer-term evolution of those classes within the OMZ. Diapycnal oxygen fluxes (ϕ_{O_2}; see Methods) quantify oxygen redistribution, while their vertical convergence ($-\nabla_z \phi_{O_2}$) determines the mixing-driven oxygen accumulation and loss. Our observations show that oxygen supplied by the different sources is redistributed differently across oxygen classes, producing contrasting patterns of oxygen gain and loss within the Arabian Sea OMZ.

Diapycnal oxygen fluxes are highly variable, spatially patchy and intermittent (Fig. 3a) as a combination of both the variable mixing regime and oxygen gradients. Within the DCM, localized downward fluxes develop across the upper OMZ boundary, where strong oxygen gradients coincide with thin DDC-favorable layers. During winter mixed-layer deepening, a coherent band of downward flux develops beneath the pycnocline, linking the ventilated ocean surface directly to the OMZ. Around PGW filaments, upward and

downward fluxes develop across sharp thermohaline gradients, redistributing oxygen from PGW into surrounding OMZ waters. The resulting spatial and temporal variability makes the mixing-driven contribution to the oxygen balance difficult to represent in models, highlighting the need for observations that resolve these rapidly evolving, small-scale structures and quantify their contribution to OMZ oxygen budgets.

The relative importance of the oxygen sources changes substantially throughout the observation period (Fig. 3b). We quantify their contribution by vertically integrating the absolute diapycnal oxygen flux, providing a measure of total redistribution independent of flux direction. During November, DCM- and PGW-associated fluxes account for ~35% and ~43% of the total, respectively. PGW becomes increasingly important through December and is the only identified source during late December and early January, whereas winter mixed-layer ventilation dominates during mid-January and early February (~51% on average). The three identified sources together account for >75% of the total oxygen redistribution, with the remaining fraction likely reflecting source-identification thresholds (see Methods) and/or transient oxygen inputs arising from local variability that are not captured by these source definitions.

Despite this seasonal shift in oxygen sources, DDC consistently accounts for ~70–80% of the total flux (Fig. 3c), reflecting its persistent co-occurrence with relatively strong oxygen gradients and moderate-to-high diffusivities. Although diapycnal fluxes redistribute oxygen vertically, oxygen-class transformation occurs only where those fluxes converge (net oxygen gain) or diverge (net oxygen loss). Their combined effect produces a patchy field of vertical oxygen-flux convergence ($-\nabla_z \phi_{O_2}$; Fig. 4a). Re-expressing this convergence in oxygen coordinates directly quantifies within which oxygen class mixing preferentially supplies or removes oxygen (Fig. 4b). Mixing-driven oxygen gain acts to contract the volume occupied by a given oxygen class, whereas oxygen loss expands it, if not counteracted by biological processes. This representation reveals a coherent oxygen-space structure that is not apparent from the depth–time section alone, showing how small-scale mixing contributes to reshape the oxygen-class structure of the OMZ.

The different oxygen sources do not ventilate the OMZ uniformly; each produces a characteristic response in oxygen space, affecting a distinct portion of the OMZ (supplementary Fig. S5). During November, oxygen produced within the DCM is redistributed from oxygen-rich waters (~140–200 μmol kg^{-1}) into the upper OMZ boundary (~50–120 μmol kg^{-1}). As the DCM weakens and the mixed layer deepens during mid-December, continued oxygen accumulation contracts the ~50–80 μmol kg^{-1} oxygen classes. PGW-driven ventilation preferentially affects the lowest oxygen classes, transferring oxygen from PGW-influenced waters (~25–40 μmol kg^{-1} for 2024-2025) into the OMZ core (<20 μmol kg^{-1}), except during a shallow late-December PGW event when redistribution extends toward the hypoxic range (~20–40 μmol kg^{-1}). By January, the deepened mixed layer directly ventilates progressively lower oxygen classes, reaching

the suboxic range (down to ~5 μmol kg^{-1}). The DCM, PGW and winter mixed-layer ventilation occur at different depths and times. DCM and deep mixed-layer ventilation likely affect the whole Arabian Sea within well-defined seasonal periods, while PGW ventilates continuously along its transport pathway[26,29,30].

To assess the role of mixing in shaping the oxygen-class structure within the OMZ, we performed an idealized diffusion experiment excluding advection and biological processes and quantified how mixing alone can change the oxygen-class probability density distribution (Fig. 5). To do so, we evolved the observed oxygen field for five years under diffusion alone, comparing a uniform diffusivity of 10^{-5} m^2s^{-1} with the observation-based composite diffusivity (K_S^{comp}; Supplementary Fig. S4) while holding each diffusivity field fixed. Both scenarios substantially modify the OMZ oxygen distribution but produce contrasting responses across oxygen classes despite identical initial conditions and conserved oxygen inventories. The uniform diffusivity scenario produces little change in probability density at oxygen concentrations of 10-15 μmol kg^{-1}, whereas the observation-based diffusivity increases it up to ~50% relative to the initial state. Conversely, moderately oxygenated waters between 20-50 μmol kg^{-1}, probability density increases by ~100% under uniform diffusivity, with moderately to no change on the observation-based diffusivity experiment. These results highlight the need to represent the covariance of the different mixing processes and oxygen gradients at small scales to accurately resolve how and where different oxygen classes of the OMZ are ventilated.

Discussion

Our observations show that mixing-driven oxygen supply shapes the oxygen-class structure within the OMZ. How this supply modifies the oxygen distribution depends on both the oxygen source and the dominant mixing regime that redistributes its oxygen content. When averaged over our observation period, mixing-driven oxygen gains and losses largely compensate, resulting in a mean response close to zero (Fig. 4c). This near-zero average nevertheless masks substantial short-term variability across oxygen classes (grey shading in Fig. 4c). Such variability is particularly important within the OMZ core, where oxygen supply and microbial consumption are closely balanced even at near-zero ambient concentrations[46–48]. Although mixing-driven oxygen supply to the most oxygen-depleted waters (<20 µmol kg^{-1}) is approximately one order of magnitude smaller than supply to the hypoxic band ($O(10^{-1})$ vs $O(10^{0})$ mmol m^{-3} day^{-1}; Fig. 4c), the microbial oxygen consumption rates are of comparable magnitude[48,49]. Transient mixing-driven ventilation can therefore perturb the local oxygen balance despite its small longer-term mean. Such fluctuations could rapidly alter the balance between supply and consumption, leading to significant shifts in aerobic and anaerobic metabolisms[46,47,51], with additions of only a few hundred nanomolar sufficient to suppress anaerobic pathways[52,53]. Predicting how OMZs will evolve under climate change remains a major challenge because changes in oxygen supply, solubility, and biological activity do not translate into uniform changes in OMZ structure[54]. Modelling efforts instead suggest a long-term reconfiguration across oxygen classes[16,17], although it is suggested that the responses differ across basins according to OMZ geometry, circulation and climate forcing[18,54]. This variability remains unexplained as the exact physical processes behind redistribution have been largely unobserved due to the difficulty of measuring mixing and oxygen concentrations over relevant scales. In particular, understanding how oxygen gradients and oxygen diffusivity may co-vary is critical to understanding the exact patterns of redistribution.

Previous studies in the Arabian Sea have identified winter convection, PGW export and changes in thermocline depth as key processes controlling the upper OMZ structure[23,28,33,55]. Our observations directly support winter mixed-layer deepening and PGW as two dominant oxygen sources, while additionally identifying subsurface production within the DCM as a distinct seasonal source. This reveals a dual biological influence on OMZ structure: respiration removes oxygen throughout the OMZ, while photosynthetic production can produce a significant oxygen supply at its upper boundary.

The pathway-specific controls identified here are unlikely to be unique to the Arabian Sea. PGW acts as a coherent subsurface oxygen source whose influence depends on advection, mesoscale stirring[26,29,30] and subsequent redistribution by mixing. Analogous pathways operate in other OMZs. In the Bay of Bengal, the summer monsoon current ventilates the OMZ[56], whereas in the Pacific, undercurrents connect tropical and eastern

boundary systems, transporting low-oxygen waters and regulating OMZ extent[57,58]. The influence of these mechanisms on OMZ structure depends on the oxygen properties of the waters they transport, the depth at which they reach the ocean interior, and their subsequent redistribution by mixing. Climate change is expected to modify these characteristics in different ways across basins. Warming of the Arabian Gulf may shoal the PGW, potentially reducing ventilation of the OMZ interior[16,59]. Projected changes in monsoon forcing are expected to modify upper-ocean circulation and thermocline depth, altering the upper oxycline ventilation[55]. In the Pacific, projected changes in circulation, mixing rates and respiration may reorganize the transport pathways that regulate OMZ extent[17,54]. Resolving these changes remains challenging because these features evolve over seasonal to climatic timescales, interact with mesoscale circulation and small-scale mixing, and remain difficult to constrain from observations or reproduce at the correct depth and intensity in climate models.

Improving projections of OMZ evolution therefore requires resolving not only circulation pathways that supply oxygen, but also the small-scale processes that redistribute it. Increasing model resolution improves representation of large-scale circulation and meso- to submesoscale variability[19,35,57], yet much of the mixing that modifies these oxygen structures remains coarsely parameterized[35,60,61]. Our observations show that DDC accounts for more than 70% of vertical oxygen redistribution despite neither consistently producing the largest diffusivities nor occurring where oxygen gradients are strongest. Comparable contributions of DDC to diapycnal transport in other OMZs[41,64] suggest that this mechanism may be broadly important. Moreover, the contrasting oxygen-class responses arising from the two diffusivity schemes in the five-year projection experiment (Fig. 5) show that reproducing the large-scale OMZ structure alone is insufficient. Although idealized, these experiments generate changes comparable in magnitude to longer-term modeled[16,17] and observed[56] shifts in OMZ oxygen distribution, demonstrating that the representation of small-scale mixing can strongly influence the resulting oxygen-class structure. Accurate projections of future OMZ reconfiguration therefore require models to represent the local oxygen sources that shape the oxygen structure within the OMZ. They must also parameterize the distribution of small-scale mixing processes, particularly DDC, and their spatial relationship to oxygen gradients. Biases in this representation can lead to significant shifts in oxygen distribution over short time scale, even when large-scale ventilation pathways are correctly represented.

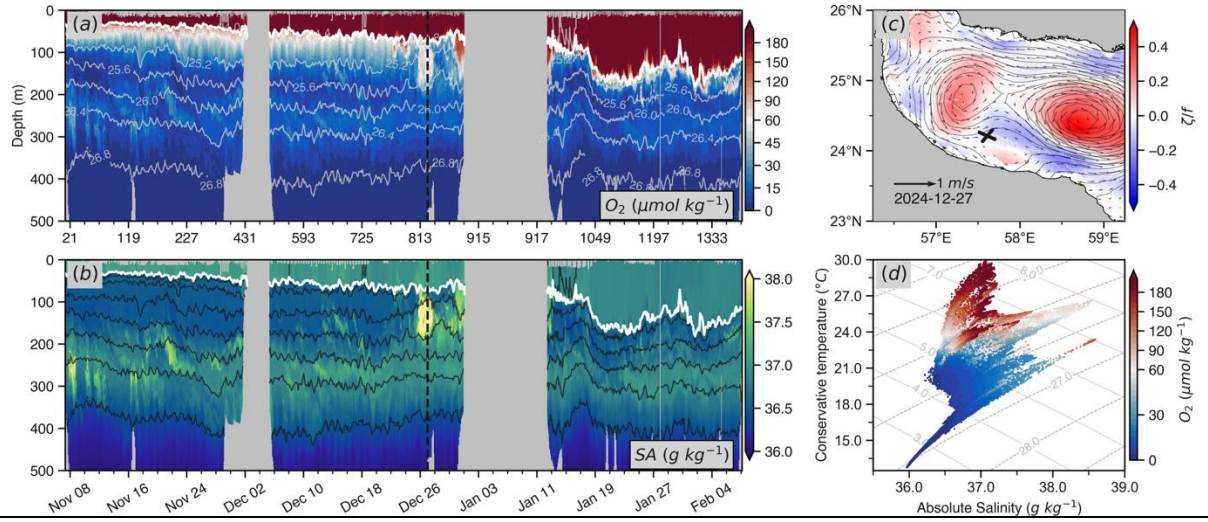


Figure 1. Hydrographic and dynamical context of the Arabian Sea oxygen minimum zone. (a) Section of dissolved oxygen concentration (μmol kg^{-1}) and (b) absolute salinity (g kg^{-1}) along the glider track. The white thick contour corresponds to the mixed-layer depth, defined using a potential density threshold of 0.125 kg m^{-3} referenced to 25 m. Isopycnals are overlaid in white in (a) and black in (b). In (a), the nonlinear color scale is used to emphasize the OMZ boundary at 60 μmol kg^{-1}. The horizontal axis shows corresponding glider profile number and time. The vertical dashed line corresponds to the timestep used shown in (c). (c) Map of the study region showing the glider sampling pattern (black cross). Colors indicate relative vorticity, thin white contours show bathymetry, arrows indicate geostrophic velocity, and solid black contours show absolute dynamic topography. (d) Absolute salinity versus conservative temperature diagram colored by dissolved oxygen concentration. Grey continued isolines denote potential density anomaly and dashed spiciness contours.

309

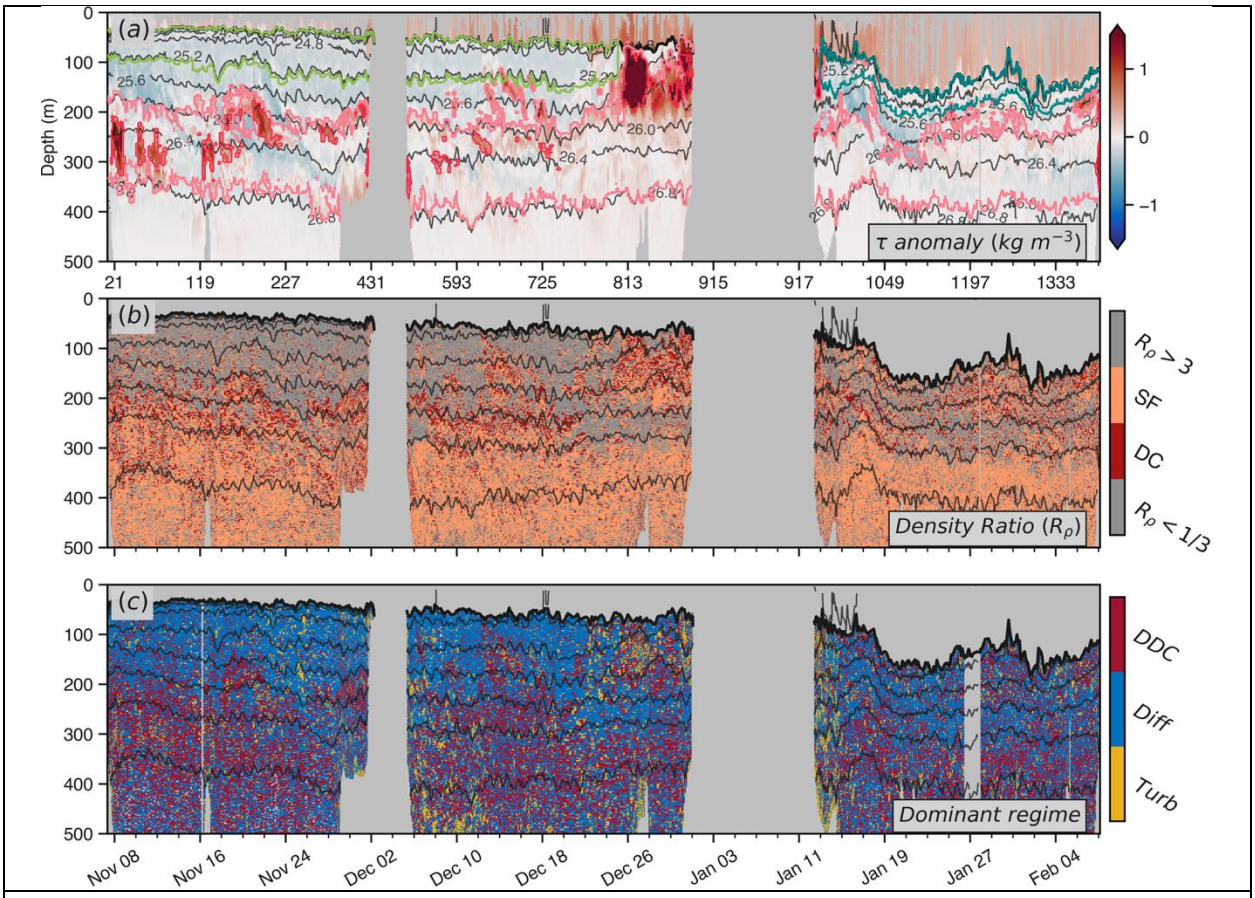


Figure 2. Water-mass structure and mixing regimes. (a) Spiciness anomaly section (kg m^{-3}), calculated as the local spiciness anomaly relative to the mean value over the observed period along each isopycnal. Green, pink and teal contours mark the deep chlorophyll maximum, Persian Gulf Water-influenced waters and deep mixed-layer regions, respectively. (b) Density ratio below the mixed-layer depth. Orange indicates salt-fingering-favorable conditions, red indicates diffusive-convective-favorable conditions, gray denotes density ratios above and below the threshold used for double-diffusive classification (see Methods). (c) Dominant mixing regime, showing double diffusive convection (red), differential mixing (blue) and shear-driven turbulence (yellow). In (a-c), black contours show potential density anomaly isopycnals and the thick black line marks the mixed-layer depth. The horizontal axis shows profile number and time.

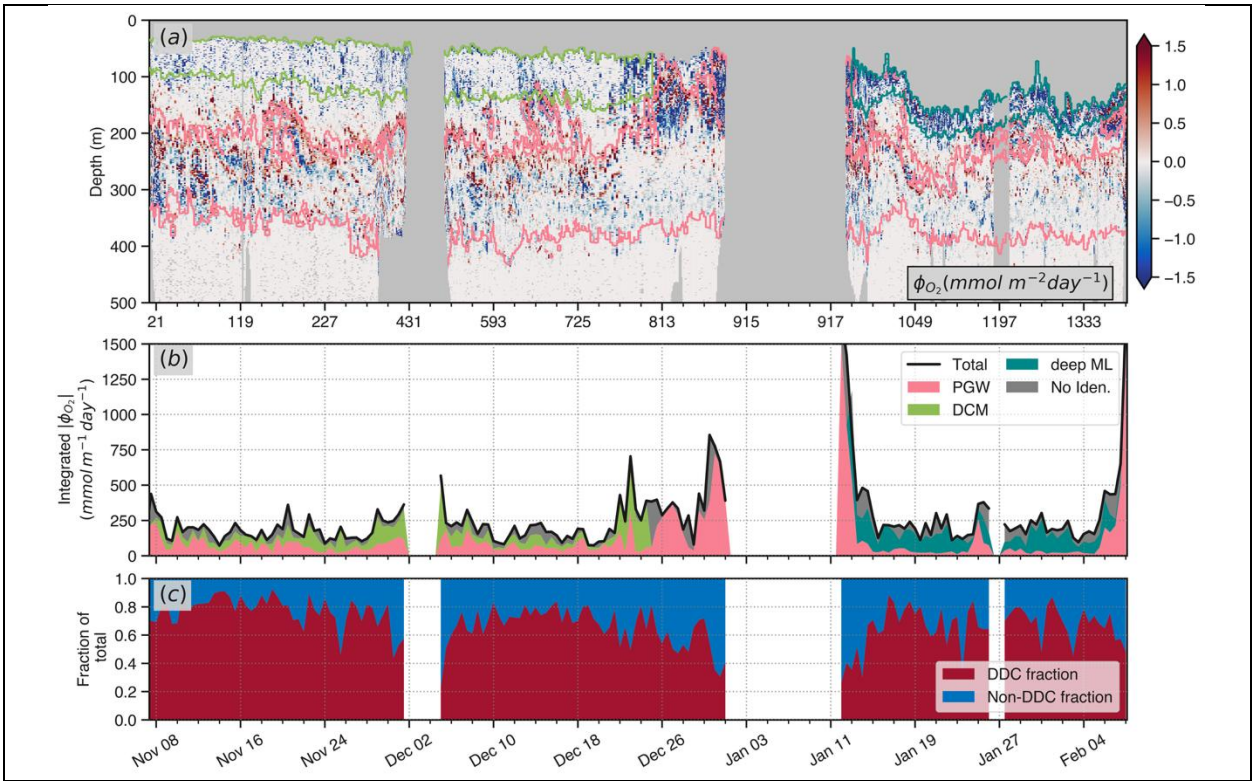


Figure 3. Oxygen fluxes below the mixed layer. (a) Diapycnal oxygen flux below the mixed-layer depth (ϕ_{O_2}; mmol m^{-2} day^{-1}). Red indicates positive, upward oxygen flux and blue indicate negative, downward oxygen flux. Green, pink and teal contours mark the deep chlorophyll maximum, Persian Gulf Water-influenced waters and deep mixed-layer regions, respectively, as in Fig. 2a. (b) Vertically integrated absolute oxygen flux, representing the total magnitude of oxygen redistribution independent of flux direction. The black line shows the total flux, and stacked shades show the contributions from the deep chlorophyll maximum (green), Persian Gulf Water-influenced waters (pink) and deep mixed-layer regions (teal); grey denotes the non-identified contribution (No Iden. = total - (DCM+PGW+Deep ML)). (c) Fraction of the total absolute oxygen flux associated with double-diffusive mixing (red) and non-double-diffusive mixing (blue). Time series in (b,c) were median-filtered using a 12-h window.

311

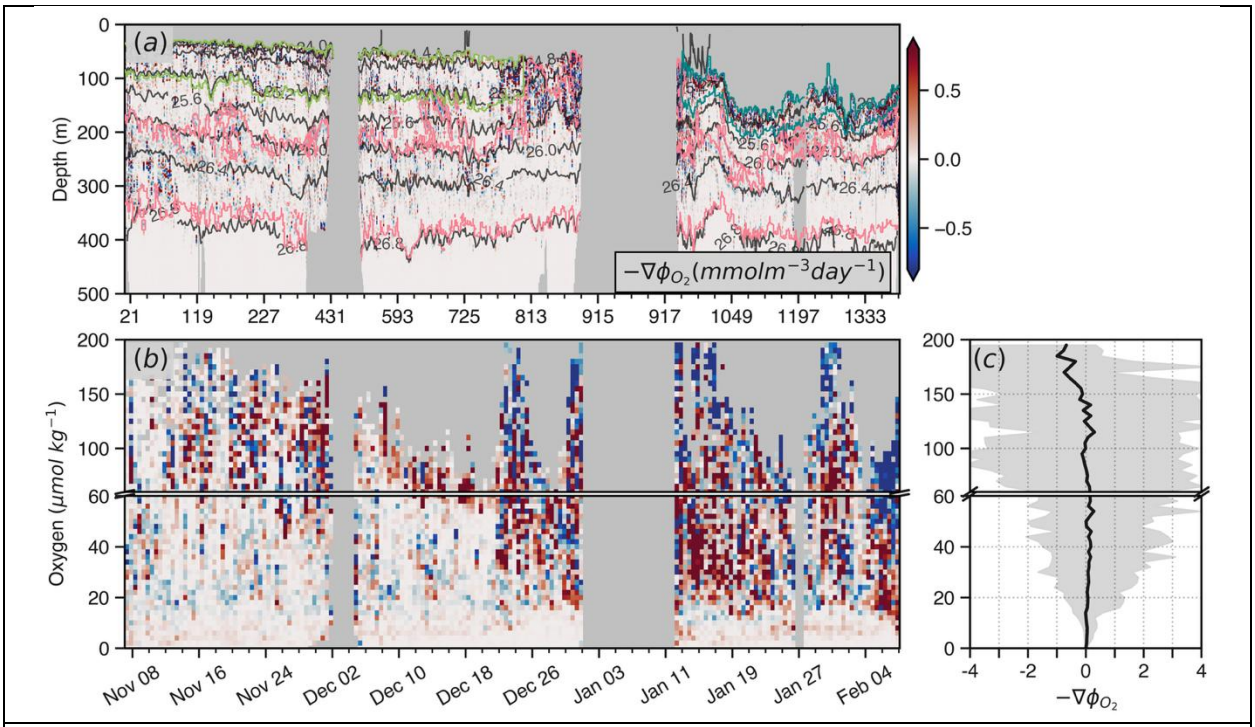


Figure 4. Mixing-driven oxygen redistribution within the oxygen minimum zone (a) Diapycnal oxygen flux convergence, $-\nabla_z \phi_{O_2}$(mmol m^{-3} day^{-1}). Red indicates oxygen gain and blue indicates oxygen loss. Green, pink and teal contours mark the deep chlorophyll maximum, Persian Gulf water-influenced waters and deep mixed-layer regions, respectively. (b) Diapycnal oxygen flux convergence regridded into oxygen space to show mixing-driven redistribution across oxygen classes. (c) Diapycnal oxygen flux convergence in oxygen coordinates averaged over the observation period. The black line shows the temporal mean, and the gray shading indicates the 3rd and 97th percentile range.

312

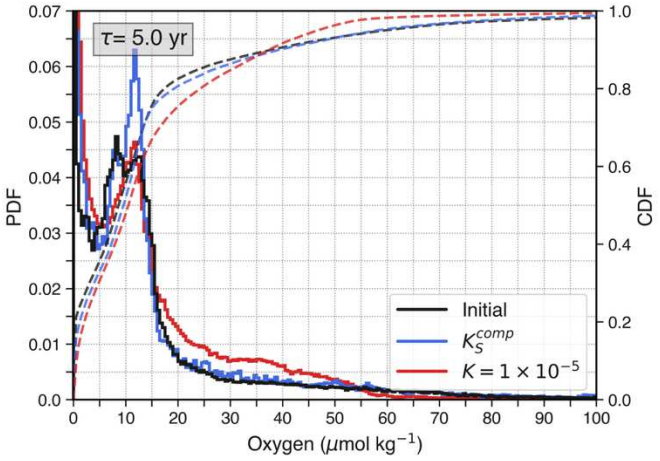


Figure 5. Small-scale mixing shapes the oxygen distribution. Probability density function (PDF, solid lines) and cumulative distribution function (CDF, dashed lines) of oxygen concentrations below the mixed layer and above 500 m depth. Black shows the observed oxygen distribution, while blue and red show the distributions after a five-year

diffusion experiment using two different diffusivity fields. Blue uses the composite diffusivity derived from our observations (see Methods), whereas red uses a uniform diffusivity of 10^{-5} m^2 s^{-1}.

References

1. Karstensen, J., Stramma, L. & Visbeck, M. Oxygen minimum zones in the eastern tropical Atlantic and Pacific oceans. *Prog Ocean.* **77**, 331–350 (2008).
2. Portela, E. *et al.* The Ocean's Meridional Oxygen Transport. *J. Geophys. Res. Oceans* **129**, e2023JC020259 (2024).
3. Lévy, M., Resplandy, L., Palter, J. B., Couespel, D. & Lachkar, Z. The crucial contribution of mixing to present and future ocean oxygen distribution. *Ocean Mix. Driv. Mech. Impacts* 329–344 (2022) doi:10.1016/B978-0-12-821512-8.00020-7.
4. Stramma, L., Johnson, G. C., Sprintall, J. & Mohrholz, V. Expanding oxygen-minimum zones in the tropical oceans. *Science* **320**, 655–658 (2008).
5. Robinson, C. Microbial Respiration, the Engine of Ocean Deoxygenation. *Front. Mar. Sci.* **5**, (2019).
6. Breitburg, D. *et al.* Declining oxygen in the global ocean and coastal waters. *Science* **359**, eaam7240 (2018).
7. Davila, X. *et al.* On the Origins of Open Ocean Oxygen Minimum Zones. *J. Geophys. Res. Oceans* **128**, e2023JC019677 (2023).
8. Lam, P. & Kuypers, M. M. M. Microbial Nitrogen Cycling Processes in Oxygen Minimum Zones. *Annu. Rev. Mar. Sci.* **3**, 317–345 (2011).
9. Diaz, R. J. & Rosenberg, R. Spreading Dead Zones and Consequences for Marine Ecosystems. *Science* **321**, 926–929 (2008).
10. Henson, S. A. *et al.* Uncertain response of ocean biological carbon export in a changing world. *Nat. Geosci.* **15**, 248–254 (2022).

11. Weber, T. & Bianchi, D. Efficient Particle Transfer to Depth in Oxygen Minimum Zones of the Pacific and Indian Oceans. *Front. Earth Sci.* **8**, (2020).

12. Ruvalcaba Baroni, I., Palastanga, V. & Slomp, C. P. Enhanced Organic Carbon Burial in Sediments of Oxygen Minimum Zones Upon Ocean Deoxygenation. *Front. Mar. Sci.* **6**, 481325–481325 (2020).

13. Ji, Q., Buitenhuis, E., Suntharalingam, P., Sarmiento, J. L. & Ward, B. B. Global nitrous oxide production determined by oxygen sensitivity of nitrification and denitrification. *Glob. Biogeochem Cycles* **32**, 1790–1802 (2018).

14. Ji, Q., Babbin, A. R., Jayakumar, A., Oleynik, S. & Ward, B. B. Nitrous oxide production by nitrification and denitrification in the Eastern Tropical South Pacific oxygen minimum zone. *Geophys Res Lett* **42**, 10,755-10,764 (2015).

15. Arévalo-Martínez, D. L., Kock, A., Löscher, C. R., Schmitz, R. A. & Bange, H. W. Massive nitrous oxide emissions from the tropical South Pacific Ocean. *Nat. Geosci.* **8**, (2015).

16. Ditkovsky, S., Resplandy, L. & Busecke, J. Unique ocean circulation pathways reshape the Indian Ocean oxygen minimum zone with warming. *Biogeosciences* **20**, 4711–4736 (2023).

17. Busecke, J. J. M., Resplandy, L., Ditkovsky, S. J. & John, J. G. Diverging Fates of the Pacific Ocean Oxygen Minimum Zone and Its Core in a Warming World. *AGU Adv.* **3**, e2021AV000470 (2022).

18. Ditkovsky, S. & Resplandy, L. Unifying Future Ocean Oxygen Projections Using an Oxygen Water Mass Framework. *J. Geophys. Res. Oceans* **130**, (2025).

19. Lachkar, Z., Smith, S., Lévy, M. & Pauluis, O. Eddies reduce denitrification and compress habitats in the Arabian Sea. *Geophys. Res. Lett.* **43**, 9148–9156 (2016).

20. Bertrand, A. *et al.* Oxygen: A fundamental property regulating pelagic ecosystem structure in the coastal southeastern tropical pacific. *PLoS ONE* **6**, (2011).

21. Naqvi, S. W. A. *et al.* Marine hypoxia/anoxia as a source of CH4 and N2O. *Biogeosciences* **7**, 2159–2190 (2010).

22. Rixen, T. *et al.* Reviews and syntheses: Present, past, and future of the oxygen minimum zone in the northern Indian Ocean. *Biogeosciences* **17**, 6051–6080 (2020).

23. Schmidt, H., Getzlaff, J., Löptien, U. & Oschlies, A. Causes of uncertainties in the representation of the Arabian Sea oxygen minimum zone in CMIP5 models. *Ocean Sci.* **17**, 1303–1320 (2021).

24. Schmidt, H., Czeschel, R. & Visbeck, M. Seasonal variability of the Arabian Sea intermediate circulation and its impact on seasonal changes of the upper oxygen minimum zone. *Ocean Sci.* **16**, 1459–1474 (2020).

25. Resplandy, L. *et al.* Controlling factors of the oxygen balance in the Arabian Sea's OMZ. *Biogeosciences* **9**, 5095–5109 (2012).

26. Queste, B. Y., Vic, C., Heywood, K. J. & Piontkovski, S. A. Physical Controls on Oxygen Distribution and Denitrification Potential in the North West Arabian Sea. *Geophys. Res. Lett.* **45**, 4143–4152 (2018).

27. Font, E., Queste, B. Y. & Swart, S. Seasonal to Intraseasonal Variability of the Upper Ocean Mixed Layer in the Gulf of Oman. *J. Geophys. Res. Oceans* **127**, (2022).

28. Shenoy, D. M. *et al*. Variability of dissolved oxygen in the Arabian Sea Oxygen Minimum Zone and its driving mechanisms. *J. Mar. Syst.* **204**, 103310 (2020).

29. L'Hégaret, P., Marez, C. de, Morvan, M., Meunier, T. & Carton, X. Spreading and Vertical Structure of the Persian Gulf and Red Sea Outflows in the Northwestern Indian Ocean. *J. Geophys. Res. Oceans* **126**, e2019JC015983-e2019JC015983 (2021).

30. Font, E. *et al*. Ventilation of the Arabian Sea oxygen minimum zone by Persian Gulf water. *J Geophys Res Oceans* **129**, (2024).

31. Midhun shah, H., Smitha, B. R., Mohamed Hatha, A. A. & Sudhakar, M. Subsurface chlorophyll maxima in the North Eastern Arabian sea: Simulation on impact of warming. *Ecol. Indic.* **110**, 105858 (2020).

32. Nampoothiri S, V. N., Sarma, Y. V. B., Rasheed, K. & Gupta, G. V. M. Influence of dynamic stability on chlorophyll distribution along the eastern Arabian Sea. *Cont. Shelf Res.* **236**, 104678 (2022).

33. Font, E., Swart, S., Vinayachandran, P. N. & Queste, B. Y. On mode water formation and erosion in the Arabian Sea: forcing mechanisms, regionality, and seasonality. *Ocean Sci.* **21**, 1349–1368 (2025).

34. Prakash, S., Nair, T. M. B., Bhaskar, T. V. S. U., Prakash, P. & Gilbert, D. Oxycline variability in the central Arabian Sea: An Argo-oxygen study. *J. Sea Res.* **71**, 1–8 (2012).

35. Bahl, A., Gnanadesikan, A. & Pradal, M.-A. Variations in Ocean Deoxygenation Across Earth System Models: Isolating the Role of Parameterized Lateral Mixing. *Glob. Biogeochem. Cycles* **33**, 703–724 (2019).

36. D'Asaro, E. A. Turbulence in the Upper-Ocean Mixed Layer. *Annu. Rev. Mar. Sci.* **6**, 101–115 (2014).

37. Ashin, K. *et al.* Double Diffusion in the Arabian Sea during Winter and Spring. *J. Phys. Oceanogr.* **52**, 1205–1231 (2022).

38. Middleton, L. & Taylor, J. R. A general criterion for the release of background potential energy through double diffusion. *J. Fluid Mech.* **893**, R3 (2020).

39. Middleton, L., Fine, E. C., MacKinnon, J. A., Alford, M. H. & Taylor, J. R. Estimating Dissipation Rates Associated With Double Diffusion. *Geophys. Res. Lett.* **48**, e2021GL092779 (2021).

40. Hamilton, J. M., Lewis, M. R. & Ruddick, B. R. Vertical fluxes of nitrate associated with salt fingers in the world's oceans. *J. Geophys. Res. Oceans* **94**, (1989).

41. Pinto-Juica, M. *et al.* Salt fingers contribute substantially to diapycnal oxygen transport into the oxygen minimum zone of the eastern South Pacific. *Commun. Earth Environ. 2026 71* **7**, 175 (2026).

42. Gregg, M. C., D'Asaro, E. A., Riley, J. J. & Kunze, E. Mixing Efficiency in the Ocean. *Annu. Rev. Mar. Sci.* **10**, 443–473 (2018).

43. Jackson, P. R. & Rehmann, C. R. Experiments on Differential Scalar Mixing in Turbulence in a Sheared, Stratified Flow. *J. Phys. Oceanogr.* **44**, 2661–2680 (2014).

44. Smyth, W. D., Nash, J. D. & Moum, J. N. Differential Diffusion in Breaking Kelvin–Helmholtz Billows. *J. Phys. Oceanogr.* **35**, 1004–1022 (2005).

45. Inoue, R., Yamazaki, H., Wolk, F., Kono, T. & Yoshida, J. An Estimation of Buoyancy Flux for a Mixture of Turbulence and Double Diffusion. *J. Phys. Oceanogr.* **37**, 611–624 (2007).

46. Zakem, E. J., Lauderdale, J. M., Schlitzer, R. & Follows, M. J. A Flux-Based Threshold for Anaerobic Activity in the Ocean. *Geophys. Res. Lett.* **48**, e2020GL090423-e2020GL090423 (2021).

47. Zakem, E. J., Mahadevan, A., Lauderdale, J. M. & Follows, M. J. Stable aerobic and anaerobic coexistence in anoxic marine zones. *ISME J.* **14**, 288–301 (2020).

48. Garcia-Robledo, E. *et al.* Cryptic oxygen cycling in anoxic marine zones. *Proc. Natl. Acad. Sci. U. S. A.* **114**, 8319–8324 (2017).

49. Robinson, C. Microbial Respiration, the Engine of Ocean Deoxygenation. *Front. Mar. Sci.* **5**, (2019).

50. Kalvelage, T. *et al.* Aerobic Microbial Respiration In Oceanic Oxygen Minimum Zones. *PLOS ONE* **10**, e0133526 (2015).

51. McCoy, D., Damien, P., Yang, S. & Bianchi, D. Mesoscale Eddy Variability Enhances Fixed Nitrogen Loss and Suppresses Nitrous Oxide Production in Oxygen Minimum Zones. *Geophys. Res. Lett.* **51**, e2023GL106179 (2024).

52. Dalsgaard, T. *et al.* Oxygen at nanomolar levels reversibly suppresses process rates and gene expression in anammox and denitrification in the oxygen minimum zone off Northern Chile. *mBio* **5**, (2014).

53. Bristow, L. A. *et al*. Ammonium and nitrite oxidation at nanomolar oxygen concentrations in oxygen minimum zone waters. *Proc. Natl. Acad. Sci. U. S. A.* **113**, 10601–10606 (2016).

54. Lachkar, Z. & Ouala, S. Expansion versus intensification: oxygen-volume distribution shapes contrasting OMZ responses to deoxygenation. *Environ. Res. Lett.* **21**, 144027 (2026).

55. Lachkar, Z., Lévy, M., Hailegeorgis, D. & Vallivattathillam, P. Differences in recent and future trends in the Arabian Sea oxygen minimum zone: processes and uncertainties. *Front. Mar. Sci.* **10**, (2023).

56. Sheehan, P. M. F., Webber, B. G. M., Sanchez-Franks, A. & Queste, B. Y. lah. *Ocean Sci.* **21**, 1575–1588 (2025).

57. Busecke, J. J. M., Resplandy, L. & Dunne, J. P. The Equatorial Undercurrent and the Oxygen Minimum Zone in the Pacific. *Geophys. Res. Lett.* **46**, 6716–6725 (2019).

58. Llanillo, P. J., Pelegrí, J. L., Talley, L. D., Peña-Izquierdo, J. & Cordero, R. R. Oxygen pathways and budget for the eastern South Pacific oxygen minimum zone. *J Geophys Res Oceans* **123**, 1722–1744 (2018).

59. Lachkar, Z., Mehari, M., Al Azhar, M., Lévy, M. & Smith, S. Fast local warming is the main driver of recent deoxygenation in the northern Arabian Sea. *Biogeosciences* **18**, 5831–5849 (2021).

60. Duteil, O. & Oschlies, A. Sensitivity of simulated extent and future evolution of marine suboxia to mixing intensity. *Geophys. Res. Lett.* **38**, (2011).

61. Takahashi, A. & Hibiya, T. Assessment of Finescale Parameterizations of Deep Ocean Mixing in the Presence of Geostrophic Current Shear: Results of Microstructure Measurements in the Antarctic Circumpolar Current Region. *J. Geophys. Res. Oceans* **124**, 135–153 (2019).

62. Brandt, P. *et al.* On the role of circulation and mixing in the ventilation of oxygen minimum zones with a focus on the eastern tropical North Atlantic. *Biogeosciences* **12**, 489–512 (2015).

63. Lueck, R. *et al.* Best practices recommendations for estimating dissipation rates from shear probes. *Front. Mar. Sci.* **11**, (2024).

64. Piccolroaz, S., Fernández-Castro, B., Toffolon, M. & Dijkstra, H. A. A multi-site, year-round turbulence microstructure atlas for the deep perialpine Lake Garda. *Sci. Data* **8**, 188 (2021).

65. Egbert, G. D. & Erofeeva, S. Y. Efficient Inverse Modeling of Barotropic Ocean Tides. *J. Atmos. Ocean. Technol.* **19**, 183–204 (2002).

66. Global Ocean Gridded L 4 Sea Surface Heights And Derived Variables Reprocessed 1993 Ongoing. https://doi.org/https://doi.org/10.48670/moi-00148.

67. McDougall, T. & Krzysik, O. Spiciness. *J. Mar. Res.* **73**, (2015).

68. McDougall, T. J. & Barker, P. M. Getting started with TEOS-10 and the Gibbs Seawater (GSW) Oceanographic Toolbox. in 28 pp. (2011).

69. Thomas, L. N., Taylor, J. R., Ferrari, R. & Joyce, T. M. Symmetric instability in the Gulf Stream. *Deep Sea Res. Part II Top. Stud. Oceanogr.* **91**, 96–110 (2013).

70. Fischer, T. *et al.* Diapycnal oxygen supply to the tropical north Atlantic oxygen minimum zone. *Biogeosciences* **10**, 5079–5093 (2013).

71. Osborn, T. Estimates of the local rate of vertical diffusion from dissipation measurements. *J Phys Ocean.* **10**, 83–89 (1980).

72. Osborn, T. R. & Cox, C. S. Oceanic fine structure. *Geophys Fluid Dyn* **3**, 321–345 (1972).

73. St Laurent, L. The contribution of salt fingers to vertical mixing in the North Atlantic tracer release experiment*. *J Phys Ocean.* **29**, 1404–1424 (1999).

74. Ledwell, J. R., Watson, A. J. & Law, C. S. Mixing of a tracer in the pycnocline. *J. Geophys. Res. Oceans* **103**, 21499–21529 (1998).

75. Storkey, D. *et al.* UK Global Ocean GO6 and GO7: a traceable hierarchy of model resolutions. *Geosci. Model Dev.* **11**, 3187–3213 (2018).

76. Wang, Q. *et al.* Impact of increased resolution on Arctic Ocean simulations in Ocean Model Intercomparison Project phase 2 (OMIP-2). *Geosci. Model Dev.* **17**, 347–379 (2024).

Online Methods

Observational campaign

The data used in this study were obtained with a SeaExplorer underwater glider (SEA057) that was deployed for three consecutive missions in the Gulf of Oman between November 2024 and February 2025. The glider was equipped with sensors for temperature, salinity (RBR Legato), chlorophyll, optical backscatter (Wetlabs EcoPuck), oxygen (AROD-FT), ADCP (Nortek AD2CP) and a microstructure turbulence sensor (Rockland MR-1000G). The deployment followed a cross-shaped pattern 25 km wide with an ~8 days of full repetition rate and covered an area spanning from the continental shelf to ~55 km offshore. Microstructure shear data were processed using Rockland Scientific ODAS Matlab® Library v4.5.1, and quality controlled (QC) with the best practices recommendations of the ATOMIX working group[63] to obtain the turbulent kinetic energy dissipation rate (ε). Only ε observations that passed all the QCs metrics (QC=0) were retained for analysis. Microstructure temperature (T_{fast}) data were processed using the Matlab® library adapted from Piccalroaz et al. (2021)[64] to obtain the thermal variance dissipation rate (χ). Since there are no best practices and recommendations for χ, we adopted a conservative workflow that mirrors our ε treatment. We applied the same segment-level QC used for ε and only permitted valid values of χ when QC=0. The 609 microstructure profiles (T_{fast}, ε and χ) were combined with the glider and ADCP time series. To enable joint analysis of hydrography, oxygen, ADCP velocities, and turbulence parameters, all variables were subsequently regridded using a 1 m bin size, matching the median vertical resolution of ε and χ.

Ocean currents were processed using the community-developed toolbox gliderad2cp (https://pypi.org/project/gliderad2cp/). Current profiles were obtained on a per dive basis (average of the up- and down-casts) and referenced to Earth coordinates by referencing to dive-averaged currents, determined via dead-reckoning using the ADCP as a doppler velocity logger. The barotropic tide was removed from the velocity profiles using the high-resolution (1/60°) TPXO Tidal Model for the Arabian Sea[65].

Sea surface height and surface geostrophic velocities were obtained from the 1/8° daily DUACS multimission altimetry product, distributed by Copernicus Marine Service[66]. This dataset was used to contextualize the mesoscale eddy field in the study region during the glider deployment, providing a synoptic view of the background circulation against which the high-resolution in situ observations are interpreted.

Hydrographic and thermohaline properties

The mixed layer depth (MLD) was defined following a density threshold criterion, using a reference depth of 25 m and a density increase 0.125 kg m^{-3} relative to that depth. These

thresholds were selected to approximate the maximum depth extension of the ε-based mixing layer while minimizing diurnal variability and define the boundary between surface-forced and subsurface forced mixing regimes.

We used spiciness to distinguish between density-compensated water masses with contrasting thermohaline properties. Spiciness was calculated using the definition in McDougall and Krzysik (2015)[67] implemented by the TEOS-10[68] *spiciness0* routine. To isolate hydrographic anomalies associated with PGW presence and its fine-scale variability, hydrographic properties (conservative temperature, oxygen concentration and spiciness) were first regridded onto potential density anomaly coordinates. At each density level, the mean value was subtracted to define an anomaly relative to the local background state. These density-space anomalies were then interpolated back to depth coordinates.

Non-dimensional parameters characterizing the dynamical and thermohaline regime were calculated, including the buoyancy Reynolds number ($\mathrm{Re_b} = \frac{\varepsilon}{\nu \mathrm{N}^2}$), the gradient Richardson number ($\mathrm{Ri} = \frac{\mathrm{N}^2}{\mathrm{U_z}^2}$), and the density ratio ($\mathrm{R_\rho} = \frac{\alpha}{\beta}\frac{\Theta_z}{\mathrm{S_z}}$). Here, ν is the kinematic viscosity, N^2 the buoyancy frequency squared, $\mathrm{U_z}$ the vertical shear of the horizontal velocity, α and β the thermal expansion coefficient and haline contraction coefficient, respectively, Θ the conservative temperature, and S the absolute salinity. The subscript z represents the vertical gradient of the variable.

Persian Gulf Water fraction

We identified the presence of Persian Gulf Water (PGW) using the water-mass fraction approach of Font et al. (2024)[30]. The method estimates the PGW contribution in Conservative Temperature–Absolute Salinity space relative to three prescribed water-mass endmembers. We defined the endmembers from practical salinity (SP) and in-situ temperature (T) as Arabian Sea Water (SP = 34.7, T = 1 °C), PGW (SP = 40.85, T = 29.8 °C), and an intermediate water endmember (SP = 36.2, T = 23.5 °C). We classified waters with a PGW fraction >0.15 as showing broader PGW influence and those with a PGW fraction >0.30 as intense coherent PGW filaments (Supplementary Fig. S1d).

Dominant mixing regime

Small-scale turbulence driving vertical mixing in the ocean can arise from multiple processes, with distinct responses for the vertical turbulent transport of heat, salt and dissolved tracers. We classify the observations into three mixing regimes: (1) energetic, weakly stratified turbulence associated with internal-wave breaking, surface wind shear, surface-driven convection and other shear-generating instabilities[69]; (2) less energetic, strongly stratified turbulence, primarily driven by the breaking of internal waves below the mixed layer, where the turbulent diffusivity of salt is weaker than the thermal; and (3)

double-diffusive convection (DDC), driven by the stirring of compensated gradients in temperature and salinity. Because each regime drives distinct turbulent diffusivities for distinct tracers, and the local diapycnal oxygen flux is equal to the product of the turbulent oxygen diffusivity and the local vertical oxygen gradient, identifying the appropriate mixing regime is essential for accurately quantifying oxygen redistribution. To estimate oxygen fluxes, we treat dissolved oxygen as salt-like tracer and assume $K_{O_2} \approx K_S$, consistent with previous estimates of diapycnal oxygen fluxes in OMZs[70]. We classify the dominant mixing regime below the mixed layer depth and over the upper 500 m of the water column using the non-dimensional parameters $\mathrm{Re_b}$, Ri, and $\mathrm{R_\rho}$.

(1) Fully developed shear-driven mixing. Under fully developed shear-driven turbulence, diapycnal eddy diffusivity ($\mathrm{K_\rho}$) was estimated following Osborn (1980)[71], assuming a local balance between shear production, viscous dissipation, and buoyancy flux. Under these conditions,

$$\mathrm{K_S^{turb}} = \Gamma \frac{\langle \varepsilon \rangle}{\overline{\mathrm{N^2}}} \quad (1)$$

where Γ is the mixing coefficient, related to the flux Richardson number ($\mathrm{R_f}$) through $\Gamma = \mathrm{R_f}/(1 - \mathrm{R_f})$. $\mathrm{R_f}$ represents the fraction of shear production that is converted into potential energy (buoyancy flux) rather than being dissipated as heat by viscosity, known as the mixing efficiency. An observationally supported upper threshold value of $\Gamma = 0.2$ was adopted[42]. The Osborn formulation assumes fully developed, homogeneous turbulence in which tracers diffuse at comparable rates ($\mathrm{K_\rho} = \mathrm{K_T} = \mathrm{K_S}$). Such conditions are typically satisfied when $\mathrm{Re_b} >> 100$ [44].

(2) Differential mixing under low $\mathbf{Re_b}$. Numerical simulations and laboratory experiments[43] show that under weak turbulence ($\mathrm{Re_b} << 100$), the eddy diffusivity of heat exceeds that of salt ($\mathrm{K_T} > \mathrm{K_S}$). This reflects the reduced efficiency of salt mixing under low-energy conditions. Under this regime, the salt diffusivity was parameterized as:

$$\mathrm{K_S^{diff}} = \mathrm{d} \cdot \mathrm{K_T} \quad (2)$$

where $\mathrm{d} = \mathrm{d}(\mathrm{Re_b})$ is an empirical function following Jackson and Rehmann (2014)[43], which accounts for the suppression of salt diffusivity under weak turbulence. The thermal diffusivity was estimated using the Osborn & Cox (1972)[72] formulation directly from the fast temperature measurements:

$$\mathrm{K_T} = \frac{1}{2} \frac{\langle \chi \rangle}{\overline{\Theta_z^2}} \quad (3)$$

(3) Double diffusive convection (DDC). Differences in the molecular diffusivities of heat and salt can generate double-diffusive instabilities by releasing available potential energy stored in compensated temperature-salinity gradients. For DDC to develop, compensated temperature-salinity gradients must persist at microscales[38]. Because microscale salinity gradients are not resolved by our observations, we assume that the microscale density ratio is represented by the meter-scale density ratio (R_ρ), following previous studies[45,73]. In the ocean, vertical temperature and salinity gradients tend to dominate, giving rise to two DDC regimes: (i) salt-fingering (SF) favorable conditions, in which warm, salty water overlies colder, fresher water ($R_\rho > 1$); and (ii) diffusive-convection (DC) favorable conditions, in which cold, fresh water overlies warmer, saltier water ($0 < R_\rho < 1$). Both regimes (SF and DC) can develop nonlinear convective instabilities. However, we do not explicitly resolve the specific turbulent instabilities; rather we assume that the turbulent dissipation (ε) is driven by turbulent buoyancy fluxes ($\overline{w'b'}$) generated by double diffusion. For this balance to hold, the energy input by shear production requires to be weak; therefore, we exclude observations with $Ri < 1$ from the DDC classification regime. In addition, as R_ρ approaches 1, temperature and salinity gradients become increasingly density-compensating, strengthening double-diffusive buoyancy fluxes in both salt-fingering and diffusive-convective favorable regimes. Because DDC is parameterized using the meter-scale density ratio, weak background salinity or temperature can produce extreme R_ρ values that may not reflect the compensated temperature-salinity gradients present at microscales. This occurs at large R_ρ for SF-favorable and as R_ρ approaches zero for DC-favorable conditions. We therefore restrict DDC regime identification to $1 < R_\rho < 3$ for salt-fingering and $1/3 < R_\rho < 1$ for diffusive-convection, following previous studies[45].

To calculate the turbulent diffusivity of salt under DDC-favorable stratification, we follow the decomposition of Hamilton at al. (1989)[40], which partitions the density flux into its thermal and haline contributions based on a linearized equation of state (their Eq. 4):

$$K_\rho \overline{N^2} = gK_T\alpha\overline{\Theta_z} - gK_S\beta\overline{S_z} \quad (4)$$

where, as for the case of Eq. 1 and 3, the turbulent density, temperature and salinity fluxes are parametrized as the product of the tracer diffusivity and their background vertical gradient ($\overline{w'\rho'} = -K_\rho\overline{N^2}$, $\overline{w'T'} = -K_T\overline{\Theta_z}$ and $\overline{w'S'} = -K_S\overline{S_z}$, respectively). Here, the subscript z denotes the vertical gradient. The thermal diffusivity is given by Eq. (3), whereas the density diffusivity is estimated from Eq. (1).

Under DDC favorable conditions ($1/3 < R_\rho < 3;\ Ri > 1$), shear production is assumed to be negligible, and the dissipation of kinetic energy is entirely balanced by the release of background potential energy. Consequently, the mixing coefficient approaches $\Gamma = -1$.

Substituting this value into Eq. (4), the turbulent diffusivity of salt under DDC-favorable stratification is parameterized as:

$$K_S^{DDC} = R_\rho \cdot K_T - \frac{\Gamma\langle\varepsilon\rangle}{\beta g \bar{S}_z} \quad (5)$$

Together, these formulations provide a consistent framework for estimating diapycnal diffusivities across distinct mixing regimes, enabling regime-dependent quantification of the oxygen redistribution. The regime-specific diffusivities were combined into a composite salt diffusivity (K_S^{comp}; Supplementary Fig. S4). At each depth and time, K_S^{comp} was assigned from the mutually exclusive parameterization for shear-driven turbulence, differential mixing, or DDC. This composite diffusivity was then used as the turbulent oxygen diffusivity. The diapycnal oxygen flux was calculated as:

$$\phi_{O_2} = -K_S^{comp}\,\overline{O_2}_z \quad (6)$$

Where $\overline{O_2}_z$ is the vertical oxygen gradient, and ϕ_{O_2} has units of mmol m^{-2} day^{-1}. Local oxygen gain or loss was quantified from the vertical convergence of this flux, $-\nabla_z\phi_{O_2}$, with positive values indicating oxygen accumulation and negative values indicating oxygen loss. In Eq. (1)-(6), $\langle\varepsilon\rangle$ and $\langle\chi\rangle$ were calculated from the measured microstructure profiles using a bootstrap approach within 11-m vertical sliding windows, and $\langle\cdot\rangle$ denotes the bootstrap mean within each sliding window. The mean vertical gradients ($\bar{\cdot}$) were computed over the same interval using linear least-squares fits. Table 1 summarizes the non-dimensional parameters used to diagnose the different mixing regimes.

Oxygen source identification

Oxygen sources were identified from their characteristic water-mass, chlorophyll and density signatures (Fig. 1a; Supplementary Fig. S1). PGW-influenced waters were defined where the estimated PGW fraction exceeded 0.15 below the mixed layer and above 500 m. The DCM was identified below the mixed layer and above the $\sigma_0 = 25.25$ kg m^{-3} isopycnal, chosen to encompass the vertical extent of the chlorophyll maximum (Supplementary Fig. S1b) and its associated oxygen signal (Fig. 1a). Winter mixed-layer ventilation was identified below the mixed layer and above $\sigma_0 = 25.4$ kg m^{-3}, chosen to approximate the deepest density surface influenced by winter ventilation (Fig. 1a). Temporal restrictions were additionally applied to separate periods dominated by each source and avoid overlap between source classifications.

Diffusion experiment

To assess the cumulative effect of the observed mixing structure on the oxygen distribution, we performed a one-dimensional vertical diffusion experiment (Fig. 5) by solving:

$$\frac{\partial O_2}{\partial t} = \frac{\partial}{\partial z}\left(K \frac{\partial O_2}{\partial z}\right), \quad (7)$$

independently for each observed profile. Oxygen and diffusivity were defined on a 1-m vertical grid, and the diffusivity field was held constant throughout each experiment. Changes in oxygen therefore represent redistribution by the prescribed vertical mixing field in the absence of additional oxygen sources or sinks.

The diffusion operator was discretized using a finite-volumes, with diffusivity evaluated at cell interfaces using the geometric mean of adjacent values. Zero-flux boundary conditions were imposed at the upper and lower limits of each valid profile, conserving the vertically integrated oxygen inventory. Because diffusivity was constant in time, the resulting linear system was integrated directly using the matrix-exponential solution, avoiding the need to specify a numerical time step. Profiles were treated independently, and only contiguous depth intervals containing valid oxygen and diffusivity values were included.

Each profile was integrated for five years using either the composite diffusivity field derived from the observations (K_S^{comp}) or a vertical uniform diffusivity of 10^{-5} m^2 s^{-1}, representative of background diapycnal mixing inferred from tracer-release experiments, microstructure observations[73,74] and commonly used as background mixing in ocean-model parameterizations[75,76]. These background estimates integrate mixing over broader spatial or temporal scales and therefore could misrepresent the strong local variability of the different mixing regimes. The same initial oxygen field and boundary conditions were used in both experiments. Solutions were required to remain non-negative, and conservation of the vertically integrated oxygen inventory was verified for each profile.

Table 1. Classification criteria for the dominant mixing regimes. Regimes were assigned using mutually exclusive masks were applied below the mixed-layer depth and within the upper 500 m of the water column, focusing the analysis on subsurface mixing processes above and within the upper Arabian Sea OMZ. Double-diffusive convection (DDC), including salt-fingering (SF) and diffusive-convection (DC) was identified for $Re_b < 100$, $Ri > 1$ and $1/3 < R_\rho < 3$. Non-DDC observations ($Ri < 1$; $R_\rho < 1/3 \cup 3 < R_\rho$) were classified as differential mixing for $Re_b < 100$ and shear-driven turbulence for $Re_b > 100$.

Mixing regime	Criteria

(1) Shear-driven turbulence		$\mathrm{Re_b} > 100$ Non-DDC
(2) Differential mixing		$\mathrm{Re_b} < 100$ Non-DDC
(3) Double diffusive convection	Salt-fingering	$\mathrm{Re_b} < 100$ $\mathrm{Ri} > 1$ $1/3 < \mathrm{R_\rho} < 1$
	Diffusive convection	$\mathrm{Re_b} < 100$ $\mathrm{Ri} > 1$ $1 < \mathrm{R_\rho} < 3$

Data availability

All quality-controlled underwater glider data that support the findings of this study, including CTD-O, currents and microstructure measurements are available via Zenodo at https://doi.org/10.5281/zenodo.22650492.

Code availability

All codes used for data processing, analysis, and figure generation in this study are publicly available via GitHub at https://github.com/maupintj/Arabian-sea-omz-mixing.

References

Acknowledgements

We are grateful to Dr. Gerd Bruss and Bader Al-Bwaiqi at Sultan Qaboos University for supporting field efforts. We thank Voice of the Ocean Foundation technical staff for their time, workspace and help ballasting gliders. We thank Rockland Scientific for staff time dedicated to support the data collection campaigns and interpretation of the microstructure measurements.

Author contributions

BQ, MP and EF conceptualized the study and collected the data. LM and AtD provided expertise developing the diffusivity parameterization and data processing. MP performed the data curation, formal analysis and wrote the manuscript draft with input from all authors.

Funding

MP and BYQ are supported by Formas grant 2022-01536. BYQ has received funding from the European Union's Horizon Europe ERC Synergy Grant programme under grant agreement No 101118693 – RECLESS. EF and BYQ were also supported by ONR GLOBAL Grant N62909-21-1-2008, the Omani Research Council grants EG/AGR/FISH/14/01 and IG/AGR/FISH/17/01. EF is now supported by Schmidt Sciences, LLC. LM is supported by Vetenskapsrådet grant 2021-00595. AtD is supported through a Research and Innovation budget allocation by Rockland Scientific.

Views and opinions expressed are those of the author(s) only and do not necessarily reflect those of the European Union or European Research Council Executive Agency. Neither the European Union nor the granting authority can be held responsible for them.

Supplementary Files

This is a list of supplementary files associated with this preprint. Click to download.

- SupplementaryMaterial20260916.docx